A 6.78-MHz Multiple-Transmitter Wireless Power Transfer System With Efficiency Maximization by Adaptive Magnetic Field Adder IC

Hao Qiu, *Member, IEEE*, Takayasu Sakurai, *Life Fellow, IEEE*, and Makoto Takamiya, *Senior Member, IEEE*

***Abstract*— A 6.78-MHz multiple-transmitter (TX) wireless power transfer (WPT) system was presented. An adaptive magnetic field adder (AMFA) IC was proposed, for the first time, to enable the maximization of the system efficiency (η_{SYS}) by adaptively optimizing the amplitude and phase of the current in each TX coil on the basis of the coupling coefficient (k) between each TX coil and the receiver (RX) coil. Under the optimal condition, the current in each TX coil is proportional to k between the TX coil and the RX coil. For the independent control of the current in each TX coil, a selectively activated shared-half-bridge (HB) power amplifier (PA) together with an alternate TX coil array was proposed. To sense a small k, duty-ratio control was proposed in the integrated k sensor. The AMFA IC was fabricated by a 0.18-μm CMOS process with 1.8-V devices. The peak power conversion efficiency of the proposed PA reached 74%. The k sensor could accurately measure k with a percentage error within ±2.5%. A WPT system consisting of a 4 × 4 TX coil array driven by four AMFA ICs and a single RX coil was implemented. Experimental results showed that, compared with the conventional system, η_{SYS} was increased from 0.11% to 51% with a load power of 576 mW when the RX coil was perpendicular to the TX coils. When the RX coil was parallel to the TX coils, a η_{SYS} of 63%, which is higher than those in previous works, was also achieved.**

***Index Terms*— Adaptive magnetic field adder (AMFA), alternate coil array, amplitude and phase control, coupling coefficient sensor, double-off control, duty-ratio control, efficiency maximization, magnetic resonance coupling, multiple transmitter (TX) coils, near field, power amplifier (PA) topology for multiple TX coils, shared topology, wireless power transfer (WPT).**

I. Introduction

WIRELESS power transfer (WPT) based on magnetic resonance coupling is a promising technology for the charging of mobile devices, including mobile phones, smart watches, and so on [1]. Instead of inserting the charging cable and leaving the devices in a corner every time, we would be able to operate them and move freely if they could be wirelessly charged; this would greatly improve the user experience.

Manuscript received 13 March 2021; revised 25 September 2021; accepted 3 June 2022. Date of publication 23 June 2022; date of current version 25 July 2022. This article was approved by Associate Editor Wing-Hung Ki. *(Corresponding author: Hao Qiu.)*

Hao Qiu is with the School of Electronic Science and Engineering, and the Engineering Research Center of Opto-Electro Materials and Chip Techniques, Nanjing University, Nanjing 210023, China (e-mail: haoqiu@nju.edu.cn).

Takayasu Sakurai and Makoto Takamiya are with the Institute of Industrial Science, The University of Tokyo, Tokyo 153-8505, Japan (e-mail: mtaka@iis.u-tokyo.ac.jp).

Color versions of one or more figures in this article are available at https://doi.org/10.1109/JSSC.2022.3183174.

Digital Object Identifier 10.1109/JSSC.2022.3183174

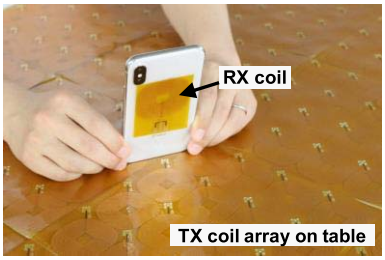

Fig. 1. WPT scenario where a mobile device with the RX coil is wirelessly charged by the TX coil array placed on a table.

To realize this vision where the receiver (RX) can change its position and sometimes be perpendicular to the transmitter (TX), many related works have been published. In a WPT system, the most important target has been the improvement of its efficiency and robustness against the variation in the position of the RX relative to the TX.

In a system using a single TX coil, the power transferred through the magnetic field is highly directional and its value drops very rapidly with distance and misalignment between the TX and RX coils. As a result, it is always required that the RX coil be perfectly aligned with the TX coil, which degrades the user experience. To alleviate this problem, several methods, such as coil design [2]–[4], new compensation topologies [5]–[7], new circuit topologies [8]–[12], and impedance matching techniques [13]–[16], have been proposed. However, when the coupling coefficient (k) between the TX and RX coils is small, the benefits that these methods yield can be limited. Under an extreme condition where k is zero, no power can be transferred to the RX coil. Physically, this case corresponds to the RX coil being perpendicular to the TX coil with the center of the TX coil being on the plane of the RX coil [17].

Rather than using a single TX coil, the system in which multiple TX coils [18]–[27] are used has gathered much attention, owing to its increased design freedom. Fig. 1 shows an application scenario in which a mobile phone is charged using multiple TX coils on a table. The conventional methods include selectively driving one of the multiple TX coils [18], [19], as shown in Fig. 2(a), and driving all TX coils with the same current [20], as shown in Fig. 2(b). On the other hand, as shown in Fig. 2(c), with the optimal control of the amplitude and phase of the current in each TX coil, the magnetic fields from multiple TX coils can be constructively added at the position of the RX coil to maximize the system

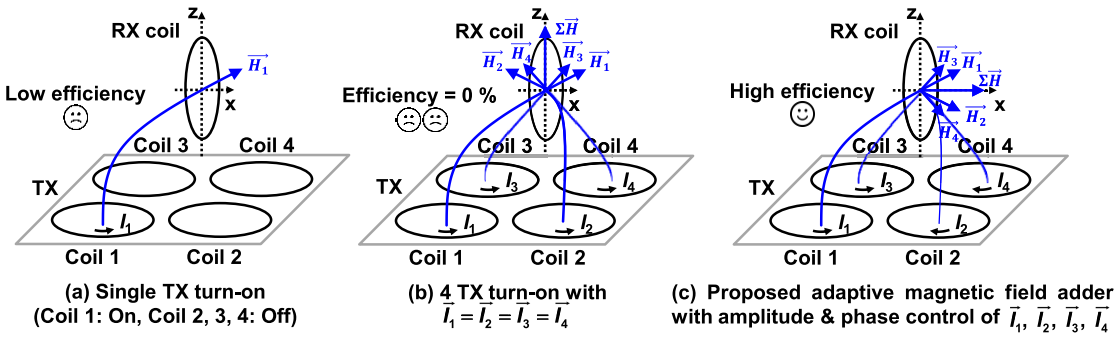

Fig. 2. Schematic of a WPT system using (a) and (b) conventional methods and (c) proposed method.

efficiency (η_{SYS}). We refer to this concept as adaptive magnetic field adder (AMFA) and its effectiveness has been theoretically demonstrated in [21]. There are two basic requirements: 1) the amplitude and phase of the current in each TX coil should be able to be independently controlled and 2) k between each TX coil and the RX coil should be adaptively measured in accordance with the position of the RX coil.

There have been several attempts to implement AMFA. It has been demonstrated that η_{SYS} can be improved [22] and the load power can be adjusted [23], [24] through the phase control of the current in each TX coil. However, no amplitude control has been discussed. In [25], it was concluded that η_{SYS} is affected by the amplitude and phase of the current in each TX coil. However, the optimal condition for attaining the maximum η_{SYS} has not been discussed. In all previous works [26]–[28], AMFA has been implemented with discrete components, which makes the system bulky and costly. Moreover, the number of power amplifiers (PAs) equals that of TX coils, which leads to a large form factor and high cost of the entire system. Furthermore, k sensing was performed using a vector network analyzer (VNA) during the experiment in [22] or even before the experiment [25], [28], which is difficult to accomplish in real applications.

Our major contributions in this work are summarized as follows.

1) For the first time, we proposed an AMFA IC in a multiple-TX WPT system that enables maximization of η_{SYS} by optimizing the amplitude and phase of the current in each TX coil.
2) The independent control of the current in each TX coil is achieved with the proposed selectively activated shared-half-bridge (HB) PA together with an alternate TX coil array. The PA topology significantly reduces the form factor.
3) In the integrated k sensor, duty-ratio control is proposed to guarantee its correct operation when measuring a small k.

Compared with our earlier work [29], herein, we added a detailed analysis as well as simulation results of the proposed PA topology and integrated k sensor, measurement results of the integrated k sensor, and a comprehensive measurement of the WPT system for different positions of the RX coil.

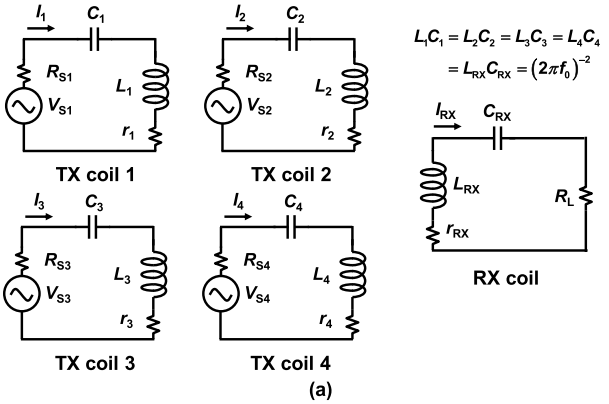

TX coil 1	TX coil 2	TX coil 3	TX coil 4	RX coil	Coupling coefficient
	k_{12}	k_{13}	k_{14}	k_1	TX coil 1
		k_{23}	k_{24}	k_2	TX coil 2
			k_{34}	k_3	TX coil 3
				k_4	TX coil 4
					RX coil

(b)

Fig. 3. (a) Equivalent circuits of the WPT system shown in Fig. 2(c). (b) Corresponding k between each pair of coils in the WPT system.

The rest of this article is organized as follows. In Section II, the multiple-TX WPT system and the control algorithm for the AMFA in it are presented. Section III shows the circuit implementation of the proposed AMFA IC. In Section IV, measurement results are presented and discussed. Finally, conclusions are given in Section V.

II. Proposed Multiple-TX WPT System

A. Control Algorithm for AMFA

Fig. 3(a) shows the equivalent circuit of the WPT system shown in Fig. 2(c). The TX side consists of four TX coils (TX coils 1–4). TX coil i ($i = 1-4$) is represented by an inductor (L_i) with a parasitic resistance (r_i) connected to a compensation capacitor (C_i) in series. The voltage source is represented by V_{Si} with an internal resistance (R_{Si}). The current flowing in TX coil i is I_i. L_{RX} and r_{RX}, respectively, represent the inductance and parasitic resistance of the RX coil. C_{RX}

is the value of the compensation capacitor. R_L is the load resistance. The current flowing in the RX coil is I_{RX}. All TX and RX coils resonate at the same resonance frequency (f_0). Fig. 3(b) shows k between each pair of coils. k_{mn} represents k between TX coils m and n, where m and n range from 1 to 4 and $m \neq n$. k_i represents k between TX coil i and the RX coil.

Applying Kirchhoff's law to the circuit, we can obtain (1), as shown at the bottom of the page. As is pointed out theoretically [21], the maximal coil-to-coil efficiency can be obtained by optimizing the amplitude and phase of the current in each TX coil. In this work, the polarity (POL) of k is also considered [30]. Under the optimized condition, for TX coil i, I_i is proportional to k_i. For example, if a positive k_1 has twice the amplitude of a negative k_2, it is required that the amplitude of I_1 is twice that of I_2 and these two currents are in antiphase. Under the optimized condition, the maximal coil-to-coil efficiency is derived as (2), shown at the bottom of the page. k between TX coils is not shown in (2) and thus does not affect the system performance.

On the other hand, if only a single TX coil, such as TX coil 1, is driven to transfer power wirelessly to the RX coil, the coil-to-coil efficiency is expressed as

$$\eta_{\text{single-TX}} = \frac{R_L \omega_0^2 k_1^2 L_1 L_{\mathrm{RX}}}{(R_L + r_{\mathrm{RX}})^2 r_1 + (R_L + r_{\mathrm{RX}}) \omega_0^2 k_1^2 L_1 L_{\mathrm{RX}}}. \quad (3)$$

To compare the coil-to-coil efficiency of a WPT system using multiple TX coils and that using a single TX coil, we performed a simple calculation. The results for (2) and (3) are shown in Fig. 4. In our calculation, for s implicity, we assume that all TX coils and the RX coil are the same. This means that all the inductances, parasitic resistances, and compensation capacitances, represented by L_0, r_0, and C_0, respectively, are the same. The values used for the calculation are shown in Fig. 4 (table inset). In addition, all k values between each TX coil and the RX coil are the same. Here, it is represented by k_0. According to the calculation results, under all coupling conditions, the coil-to-coil efficiency can be improved by using multiple TX coils compared with using a single TX coil.

As is discussed in [21], it is important to know k between each TX coil and the RX coil. On the other hand, in two recently published works [26], [27], it is claimed that the control can be realized by equalizing the input impedance of each TX coil, whereby their system implementation becomes much simpler. This conclusion is arrived at under the assumption that no coupling occurs among TX coils [26] or that an LCC inverter is used on the TX side [27], which does not represent the usual situation in WPT systems. Thus, to cover most multiple-TX WPT systems, it is still necessary to know k between each TX coil and the RX coil.

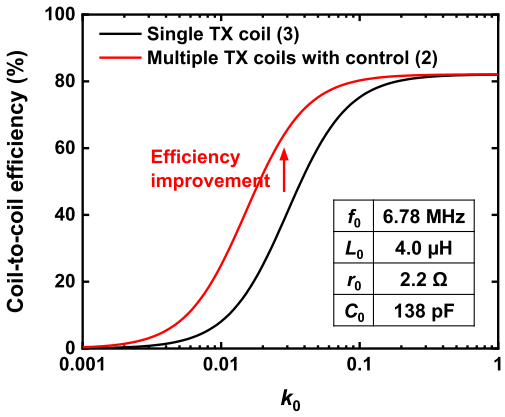

Fig. 4. Calculated coil-to-coil efficiency using a single TX coil and multiple TX coils with control.

B. System Architecture and Its Operation

The overall architecture of the proposed multiple-TX WPT system is shown in Fig. 5. It consists of four AMFA ICs, 16 TX coils, one RX coil, and a LabVIEW control block. All coils resonate at the same f_0. Each AMFA IC is connected to four TX coils, among which a single TX coil is selected to be driven. Thus, with four AMFA ICs, four TX coils in total are driven simultaneously to transfer power wirelessly to the RX coil. In this work, since the focus is put on the design of the TX side, we choose to implement the RX side in a simple way without adding a rectifier.

The operation of the WPT system has the following three steps. First, the AMFA ICs operate in the k-sensing mode. Take AMFA IC TX1 as an example. The k values between TX coils 1A–1D and the RX coil are measured, and the TX coil

$$\begin{pmatrix} V_{S1} \\ V_{S2} \\ V_{S3} \\ V_{S4} \\ 0 \end{pmatrix} = \begin{pmatrix} R_{S1}+r_1 & j\omega_0 k_{12}\sqrt{L_1 L_2} & j\omega_0 k_{13}\sqrt{L_1 L_3} & j\omega_0 k_{14}\sqrt{L_1 L_4} & -j\omega_0 k_1\sqrt{L_1 L_{\mathrm{RX}}} \\ j\omega_0 k_{12}\sqrt{L_1 L_2} & R_{S2}+r_2 & j\omega_0 k_{23}\sqrt{L_2 L_3} & j\omega_0 k_{24}\sqrt{L_2 L_4} & -j\omega_0 k_2\sqrt{L_2 L_{\mathrm{RX}}} \\ j\omega_0 k_{13}\sqrt{L_1 L_3} & j\omega_0 k_{23}\sqrt{L_2 L_3} & R_{S3}+r_3 & j\omega_0 k_{34}\sqrt{L_3 L_4} & -j\omega_0 k_3\sqrt{L_3 L_{\mathrm{RX}}} \\ j\omega_0 k_{14}\sqrt{L_1 L_4} & j\omega_0 k_{24}\sqrt{L_2 L_4} & j\omega_0 k_{34}\sqrt{L_3 L_4} & R_{S4}+r_4 & -j\omega_0 k_4\sqrt{L_4 L_{\mathrm{RX}}} \\ -j\omega_0 k_1\sqrt{L_1 L_{\mathrm{RX}}} & -j\omega_0 k_2\sqrt{L_2 L_{\mathrm{RX}}} & -j\omega_0 k_3\sqrt{L_3 L_{\mathrm{RX}}} & -j\omega_0 k_4\sqrt{L_4 L_{\mathrm{RX}}} & R_L+r_{\mathrm{RX}} \end{pmatrix} \begin{pmatrix} I_1 \\ I_2 \\ I_3 \\ I_4 \\ I_{\mathrm{RX}} \end{pmatrix} \quad (1)$$

where j is the imaginary unit and ω_0 is the resonant angular frequency and equals $2\pi f_0$.

$$\eta_{\text{multiple-TX}} = \frac{R_L \omega_0^2 \left(\sum_{i=1}^{4} k_i^2 L_i L_{\mathrm{RX}}\right)^2}{(R_L + r_{\mathrm{RX}})^2 \sum_{i=1}^{4} r_i k_i^2 L_i L_{\mathrm{RX}} + (R_L + r_{\mathrm{RX}}) \omega_0^2 \left(\sum_{i=1}^{4} k_i^2 L_i L_{\mathrm{RX}}\right)^2} \quad (2)$$

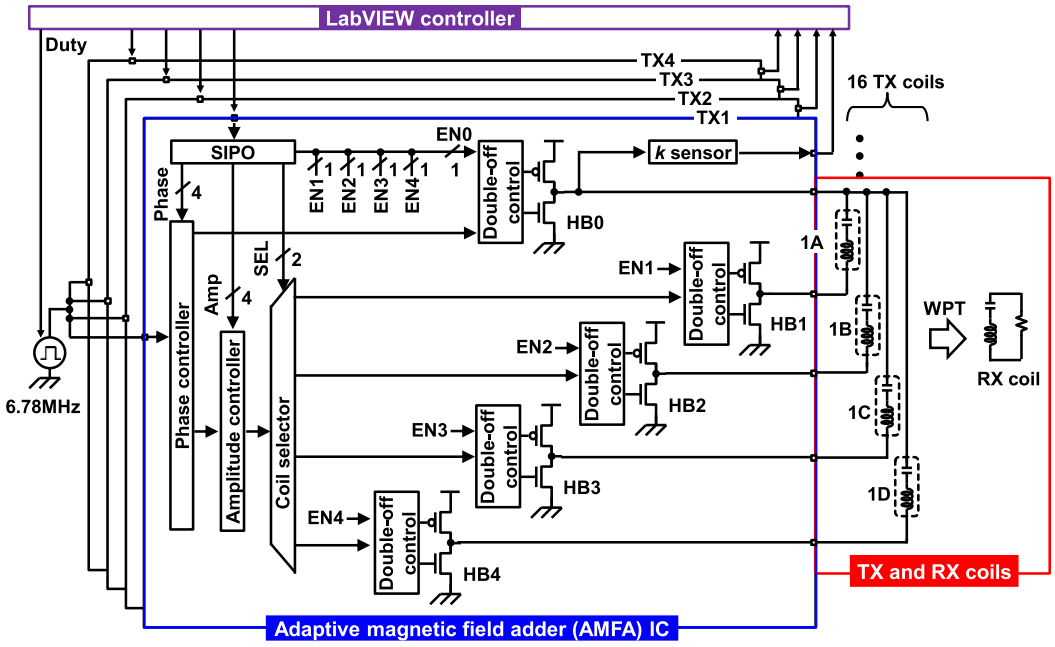

Fig. 5. Proposed WPT system consisting of AMFA ICs, TX coils, the RX coil, and a LabVIEW controller. SIPO stands for serial-in parallel-out.

with the maximum k is selected to transfer power wirelessly to the RX coil later. AMFA ICs TX2–TX4 repeat the similar procedures. Second, the k values corresponding to the selected four TX coils are transmitted to the LabVIEW block for information processing. After the information processing, the LabVIEW block generates the required control signals for the AMFA ICs and these ICs operate in the WPT mode. As will be discussed in Section III-A, the current in each TX coil is adjusted by controlling the phases of signals driving HBs in the AMFA ICs. As a result, the current in each TX coil is optimized to be proportional to k between the TX coil and the RX coil, and the coil-to-coil efficiency is maximized. Third, in a real wireless charging scenario, k can change with the change in the position of the RX coil. To adapt to this process, steps 1 and 2 are repeated at a certain interval to update the amplitude and phase of the current in each TX coil.

III. Proposed AMFA IC

As shown in Fig. 5, one AMFA IC consists of five HBs, an integrated k sensor, and digital control blocks. In this section, we describe the circuit implementation in detail.

A. PA Topology for Independent Current Control in Multiple TX Coils

In a WPT system, to reduce the power loss in PAs, one of the most important points in the design is to use power transistors with low ON resistance. Thus, the integrated power transistors in PAs are usually designed with large gate widths, resulting in occupying a large die area. This problem is considerable when we discuss the multiple-TX WPT system, in which the number of PAs equals that of TX coils. The use of an N-legged converter [31] or a multileg converter [32] has been proposed to reduce the number of power transistors. However, none of the previous methods can satisfy the requirement of our multiple-TX WPT system that the amplitude and phase of the current in each TX coil be controlled independently.

On the other hand, the current in each TX coil can be controlled independently using the proposed AMFA IC operating in the WPT mode, as is shown in Fig. 6. Fig. 6(a) shows the schematic of the proposed selectively activated shared-HB PA. Four HBs, that is, HB1–HB4, are connected to one terminal of TX coils 1A–1D, respectively. The other terminals of the four TX coils are commonly connected to a shared block, which consists of HB0 and the k sensor. Thus, the total number of HBs is five. This is a 38% reduction compared with the conventional design in which eight HBs are necessary for four TX coils. The number of k sensors is also reduced by 75%.

Among TX coils 1A–1D, only one of them is driven, whereas the other three remain idle to eliminate any possible power loss, which will be discussed later. For example, if TX coil 1A is driven, HB0 and HB1 are activated, whereas HB2–HB4 are deactivated. The amplitude and phase of the current through TX coil 1A are controlled by the phases of the signals driving HB0 and HB1 [33]. Fig. 6(b) shows the pattern of the proposed alternate TX coil array and four AMFA ICs. By combining them, we can realize the required independent control of the current in each TX coil. For example, when the RX coil is within the region indicated by the dashed square in case 1, TX coils 1A–4A are driven by AMFA ICs TX1–TX4, respectively. The same principle applies in case 2. That is, TX coils 1B, 2A, 3B, and 4A are driven by AMFA ICs TX1–TX4, respectively.

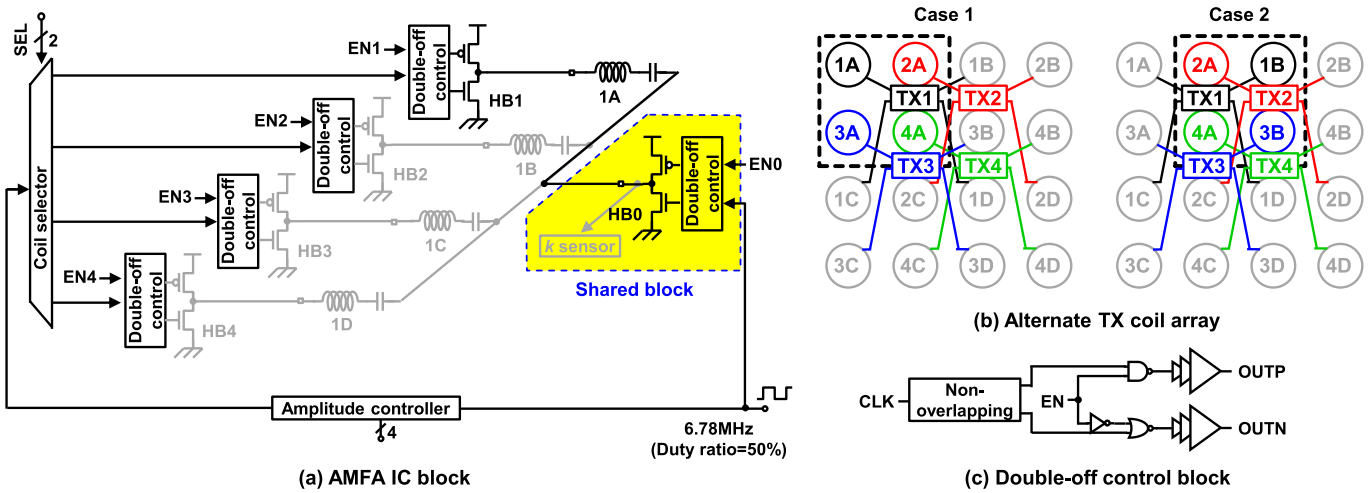

Fig. 6. AMFA IC operating in the WPT mode. (a) Proposed selectively activated shared-HB PA for the independent control of current in multiple TX coils. (b) Proposed alternate TX coil array. (c) Schematic of double-off control block.

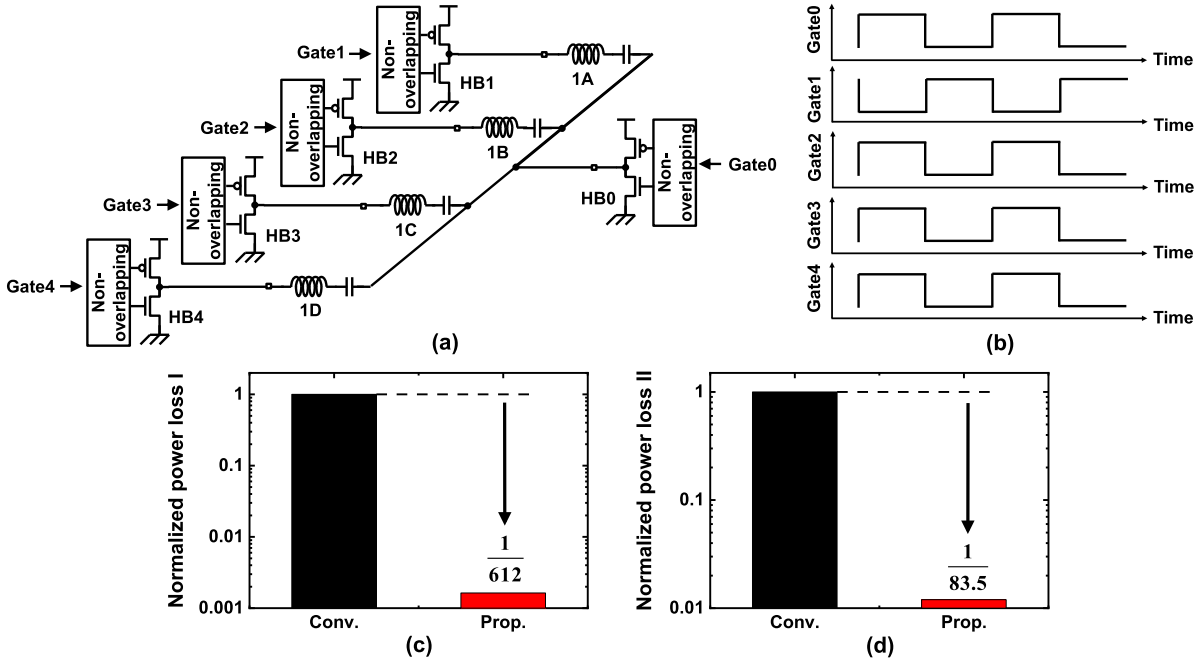

Fig. 7. (a) Schematic of PA topology obtained using the conventional control. (b) Schematic of gate drive signals to HBs. Simulated results of power losses (c) I and (d) II obtained using the conventional control and double-off control. The RX coil is assumed to be absent in the simulation.

Regarding the activation or deactivation of TX coils, Fig. 6(c) shows the schematic of the double-off control block. If the signal EN is "0," the signals connected to PMOS and NMOS in the HB are locked at "1" and "0," respectively, deactivating the HB. On the other hand, if the signal EN is "1," the HB is activated. The other way to deactivate the TX coil is to use the conventional control [31], in which the two-component HBs connected to the TX coil are activated and the corresponding gate drive signals are synchronized.

Fig. 7(a) and (b) shows an example in which TX coils 1B, 1C, and 1D are deactivated by synchronizing the corresponding gate drive signals of HB2–HB4 with that of HB0. However, two types of power loss may occur. First, the power loss can occur in deactivated TX coils, including TX coils 1B, 1C, and 1D. Take TX coil 1B as an example. The large current through TX coil 1A causes the output voltage of HB0 different from that of HB2, even when the gate drive signals of the two HBs are synchronized. The voltage difference between two terminals of TX coil 1B results in power loss, which we call power loss I. Second, all HBs are activated, resulting in power loss in the gate drivers of HB2–HB4, that is, power loss II. Different from that in the kHz range, the gate driver loss, which is proportional to the operating frequency, cannot be neglected in the MHz range.

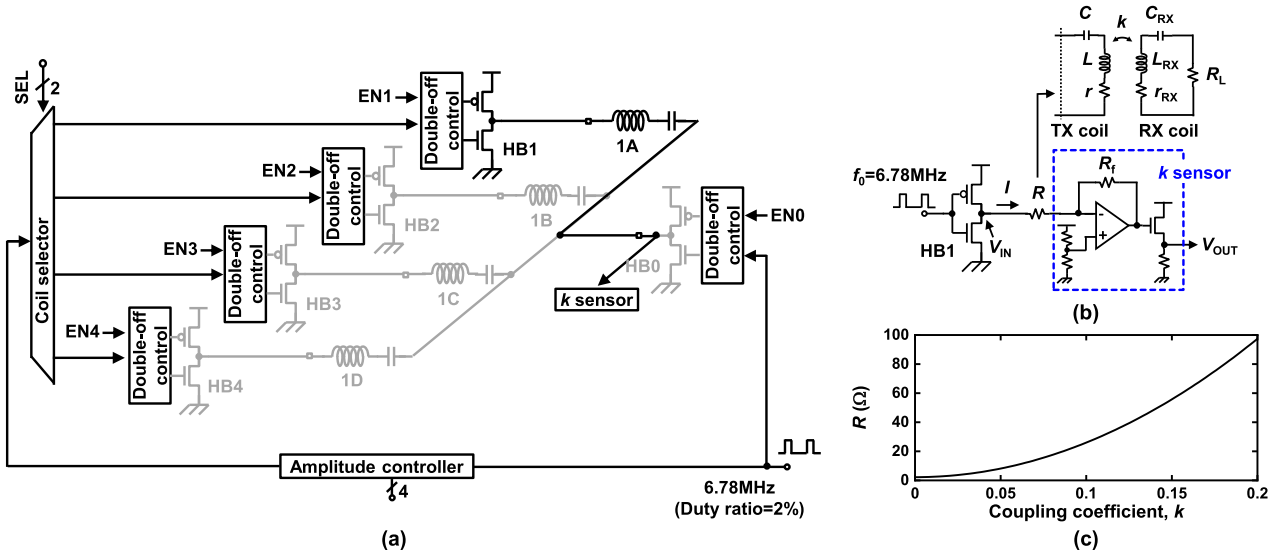

Fig. 8. Schematic of (a) AMFA IC operating in the k-sensing mode and (b) its equivalent circuit with the integrated k senor. (c) Simulated k dependence of R on the basis of (4).

Fig. 7(c) and (d), respectively, shows simulated power losses I and II obtained using the conventional control [31] and double-off control. In the simulation, the RX coil is assumed to be absent for simplicity. Power loss I obtained using the double-off control is reduced to 15.7 μW, 1/612 of the conventional value. Similarly, power loss II is reduced to 33.9 μW, 1/83.5 of the conventional value. Thus, by simply adding an additional enable signal to the conventional control, the double-off control can greatly reduce unnecessary power loss and achieve a high power conversion efficiency in the PA topology for multiple TX coils. This will be discussed again in Section IV-A. Note that the possible cause of power loss in Fig. 6(a) is the induced eddy current in TX coils other than TX coil 1A. However, this has been demonstrated to be negligible [4].

B. Integrated k Sensor and Duty-Ratio Control

The AMFA IC can also be configured to operate in the k-sensing mode to measure k between each TX coil and the RX coil. Take TX coil 1A as an example. As shown in Fig. 8(a), HB1 and the k sensor are activated by setting EN1 to "1" and all other enable signals to "0." Fig. 8(b) shows the equivalent circuit. L and r, respectively, represent the inductance and parasitic resistance of TX coil 1A. C is the value of the compensation capacitor. R is the equivalent impedance looking into TX coil 1A and equals [34]

$$R = r + \frac{\left(\omega_0 k\sqrt{LL_{\mathrm{RX}}}\right)^2}{r_{\mathrm{RX}} + R_L}. \tag{4}$$

Since f_0, L, r, L_{RX}, r_{RX}, and R_L are constants and their values are known, on the basis of (4), k can be obtained by measuring R on the TX side. Fig. 8(c) shows the simulated k dependence of R. k equals 0 when the RX coil is absent and reaches around 0.2 when the RX coil is closely coupled with the TX coil. Corresponding R values are 2.2 and 100 Ω, respectively.

This method makes k sensing much easier because the wireless communication link from the RX coil to the TX coil used in [8] is eliminated. In addition, since R is a pure resistance, rather than using a VNA [22] or a gain and phase detector [35], which is impossible to integrate, we used a simple transimpedance amplifier (TIA) for k sensor implementation.

As shown in Fig. 8(b), the current (I) supplied by HB1 flows through R, and R_f, and finally sinks in the TIA. The following equation can be derived:

$$|I| = \frac{|V_{\mathrm{IN}}|}{R} = \frac{|V_{\mathrm{OUT}}|}{\beta R_f} \tag{5}$$

where β is the voltage gain of the source follower, R_f is the feedback resistance of the operational amplifier (op-amp) in the TIA, and V_{IN} and V_{OUT} are the voltages indicated in Fig. 8(b). For small-signal analysis, $|V_{\mathrm{IN}}|$ and $|V_{\mathrm{OUT}}|$, respectively, represent the peak amplitudes of the components of V_{IN} and V_{OUT} at f_0. $|I|$ represents the peak amplitude of I. Thus, by substituting (5) into (4), we can obtain k as

$$k = \frac{\sqrt{(R_{\mathrm{RX}} + R_L)(\beta R_f |V_{\mathrm{OUT}}|/|V_{\mathrm{IN}}| - r)}}{\omega_0\sqrt{LL_{\mathrm{RX}}}}. \tag{6}$$

To guarantee the correct operation of the k sensor, two main requirements are listed for the design of the op-amp. One is that its unity-gain bandwidth should be much higher than f_0. In our design, its value is designed to be greater than ten times f_0. The other one is that the op-amp should always operate within its linear region [36]. When k is large, in other words, R is large, $|I|$ is small according to (5). Under this condition, the op-amp can operate within its linear region. On the other hand, as k decreases, R also decreases and the increased $|I|$ requirement may cause the op-amp to operate outside of its linear region [36].

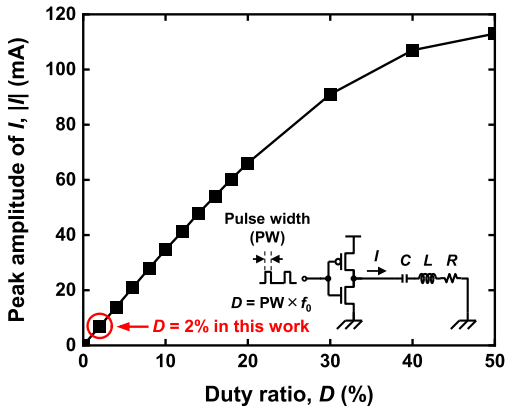

Fig. 9. Simulated dependence of the amplitude of current on D.

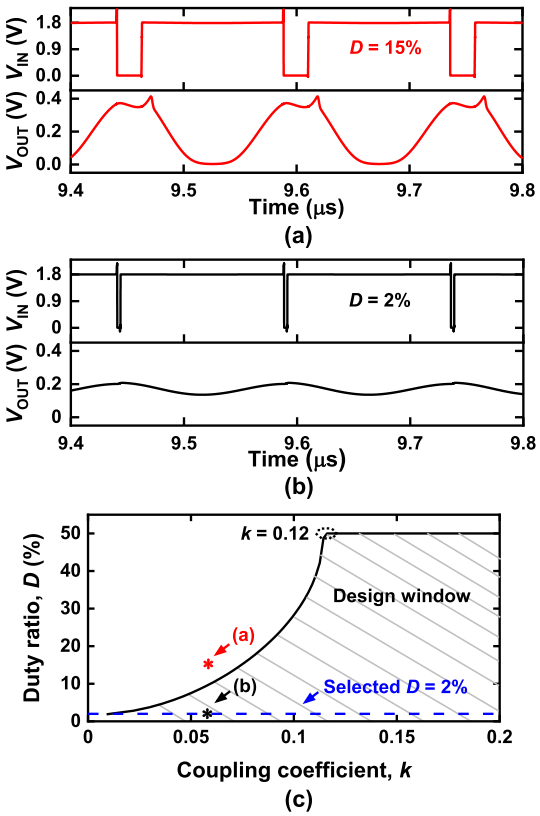

Fig. 10. Proposed duty-ratio control in the integrated k sensor. Simulated waveforms when (a) $D = 15\%$ and (b) $D = 2\%$. (c) Design window of D.

To ensure that the op-amp operates in the linear region, it is necessary to decrease $|I|$. There have been several methods of PA power control, as is reviewed in [37]. Since only a single HB is activated, the phase shift control method [38] is inapplicable. Pulse frequency modulation [39] does not comply with the requirement of the industrial, scientific, and medical (ISM) band. Instead of using pulse density modulation [40], we propose duty ratio (D) control to decrease $|I|$ when measuring a small k; this is much easier to design.

To demonstrate the capability of the proposed D control, Fig. 9 shows the simulated dependence of $|I|$ on D, in which k is assumed to be 0.058, which corresponds to

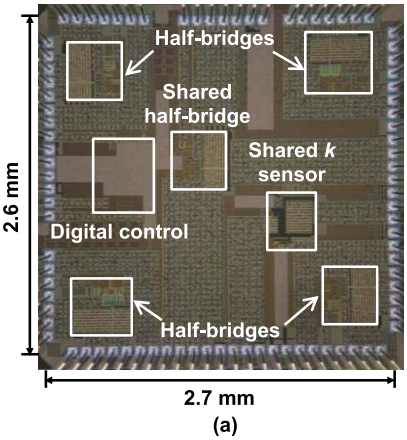

Coil specification	
Outer diameter	50 mm
Inductance	4.0 μH
Compensation capacitance	138 pF
Quality factor @ 6.78MHz	78

Fig. 11. (a) Photograph of AMFA IC. (b) Photograph and measured specifications of coil.

$R = 10\ \Omega$. As is expected, $|I|$ can be decreased by reducing D. When D is smaller than 20%, $|I|$ decreases linearly with D. Fig. 10(a) and (b) shows the simulated waveforms of V_{IN} and V_{OUT} when D equals 15% and 2%, respectively. In simulations, k and R_f are assumed to be 0.058 and 10 Ω, respectively. As was discussed before, the op-amp operates outside of its linear region and results in a distorted waveform of V_{OUT} at $D = 15\%$. On the other hand, when D becomes small, such as 2%, $|I|$ is reduced and the op-amp returns to its linear region. Fig. 10(c) shows the design window of D when using our proposed D control. When k is less than 0.12, D smaller than 50% is necessary to guarantee the correct operation of the k sensor. The black line indicates the upper limit of D as a function of k and any D within the design window can be selected. For simplicity, in this work, we select $D = 2\%$ for the k sensor. Therefore, our proposed D control guarantees correct k sensing when k is small in this work. Utilizing the k sensor, the POL of k can also be determined. The details can be referred to in the Appendix.

IV. Measurement Results

Fig. 11(a) shows the photograph of the proposed AMFA IC. Fabricated by a 1.8-V, 0.18-μm CMOS process, it occupies 7.02 mm^2. Both TX coils and the RX coil have the same parameters, as shown in Fig. 11(b). To minimize their parametric differences, we carefully tuned their f_0 to 6.78 MHz using a VNA. Fig. 12 shows the measurement setup of the proposed multiple-TX WPT system, in which four AMFA ICs (TX1–TX4) are connected to 16 TX coils, the same as shown in Fig. 6(b). The RX coil with $R_L = 10\ \Omega$ is perpendicular to TX coils.

A. AMFA IC in Two Operation Modes

We start with the measurement of the AMFA IC operating in the WPT mode. Fig. 13 (inset) shows its equivalent circuit. The phases of the signals driving HB0 and HB1 are φ_0 and φ_1, respectively. By changing their phase difference, the corresponding power conversion efficiency and output power of the AMFA IC were measured. During measurement, the supply

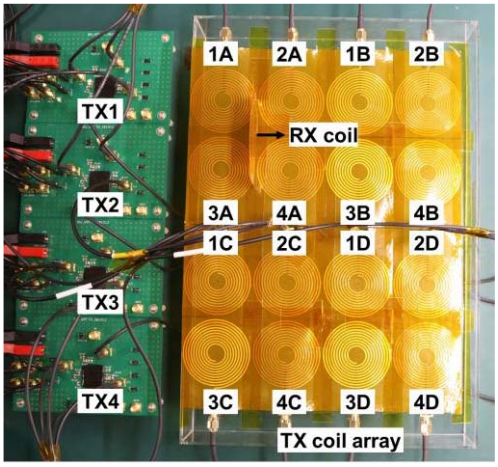

Fig. 12. Photograph of the measurement setup.

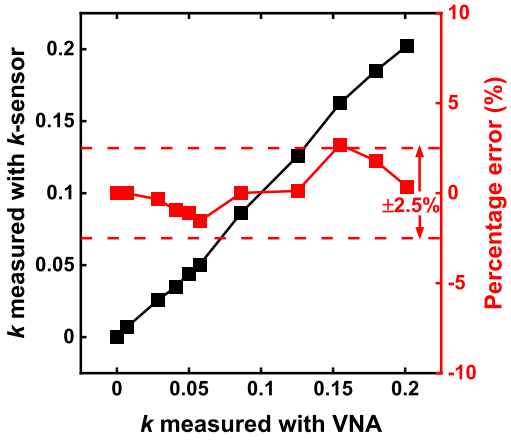

Fig. 14. Measured performance of the AMFA IC operating in the k-sensing mode.

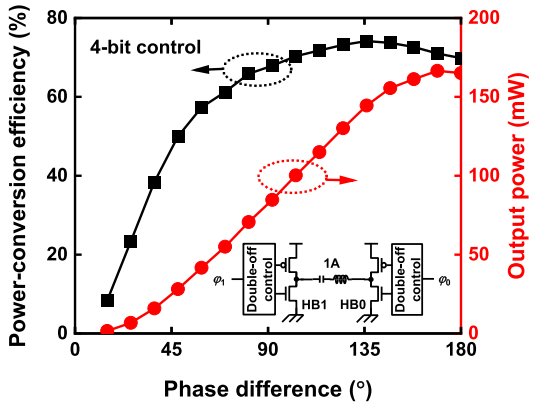

Fig. 13. Measured performance of the AMFA IC operating in the WPT mode with its equivalent circuit shown in the inset.

voltage is 1.8 V, and k between TX coil 1A and the RX coil is 0.058. The results are shown in Fig. 13.

With the four-bit control of the phase difference, the amplitude and phase of the current through TX coil 1A can be adjusted [33]. The output power shows a sinusoidal relationship with the phase difference, which is ascribed to the amplitude of the current through TX coil 1A having a sinusoidal relationship with half the phase difference [33]. When the phase difference approaches 180°, the output power shows a maximum of 167 mW. With an increase in the phase difference, the power conversion efficiency first increases and then shows a plateau where the maximum value is 74% followed by a slight decrease. The high power-conversion efficiency is owing to the double-off control in our PA topology, which is in accordance with the analysis in Section III-A. The slight decrease in power conversion efficiency when the output power approaches its maximum value is the same as the simulation results (not shown), and it may be ascribed to a larger quiescent current with respect to the output current [41].

After evaluating the AMFA IC in the WPT mode, we measured it in the k-sensing mode. As discussed previously, D was set as 2% through the entire measurement. First, we calibrated the value of βR_f in (5) when the RX coil was absent. After calibration, for each position of the RX coil, the waveforms of V_{IN} and V_{OUT} were measured and their amplitude components at f_0 were extracted by fast Fourier transform (FFT) analysis for k calculation in (6). Fig. 14 compares k measured by the k-sensor with that measured with a VNA. A good correspondence with a small percentage error within ±2.5% is demonstrated. Thus, owing to our proposed D control, k can be accurately measured by the AMFA IC.

B. System Measurement

The performance of the WPT system is evaluated in both cases shown in Fig. 6(b). In case 1, Fig. 15(a) shows the details of the coil setup, in which the RX coil is perpendicular to the TX coils. The distance from the center of the RX coil to the TX coil plane is 25 mm. Starting from the origin, the RX coil is moved along the x-direction in 12.5-mm steps.

For each position of the RX coil, as described in Section II-B, the AMFA ICs first operate in the k-sensing mode. Take AMFA IC TX1 as an example. In the k-sensing mode, this IC has two main functions. One is to detect which of the TX coils (1A–1D) has the best coupling condition with the RX coil, and the other is to know its value. Here, TX coil 1A is selected by AMFA IC TX1. Similarly, TX coils 2A–4A are selected by AMFA IC TX2–TX4, respectively. Fig. 15(b) shows the measured k between the selected TX coils (1A–4A) and the RX coil. The results for all other TX coils and the RX coil are not shown, since they are not important to the following system control. The details of how to determine the POL of k are referred to in the Appendix. After k-sensing, the AMFA ICs operate in the WPT mode. Fig. 15(c) and (d) shows the measured amplitudes and phases of the current in each TX coil, respectively. The current was measured using a current probe (Tektronix P6021).

The measurement setup is symmetric about the x-axis, and it can be expected that the coupling coefficient ($k_{1\mathrm{A}}$) between TX coil 1A and the RX coil equals that ($k_{3\mathrm{A}}$) between TX coil 3A and the RX coil and that the coupling coefficient ($k_{2\mathrm{A}}$) between TX coil 2A and the RX coil equals that ($k_{4\mathrm{A}}$) between TX coil 4A and the RX coil. In the following analysis, $k_{3\mathrm{A}}$ and

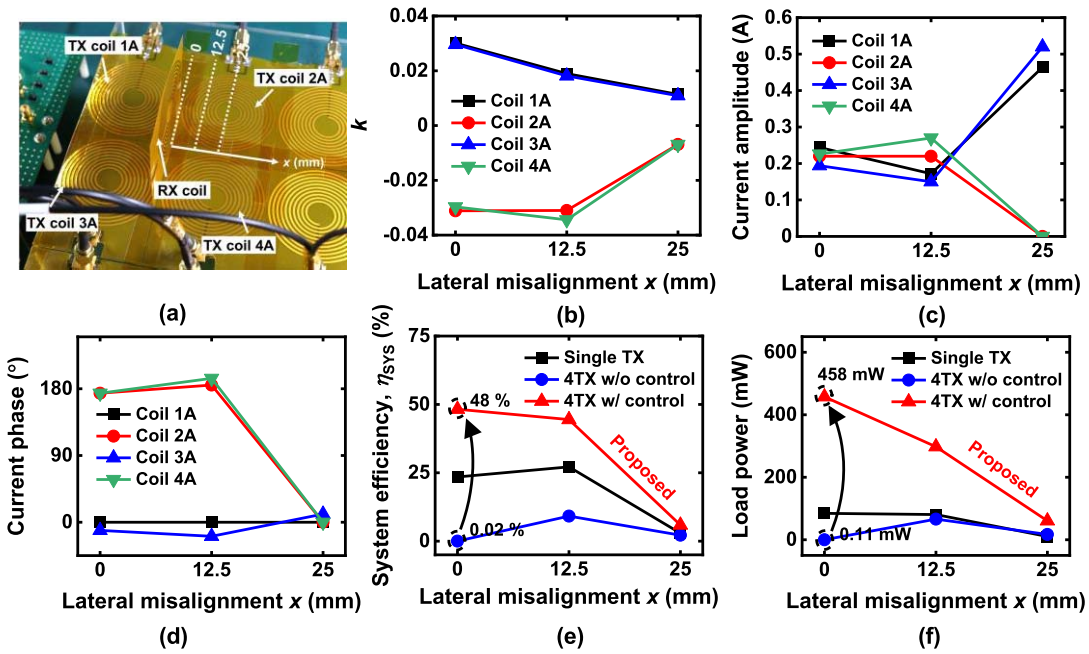

Fig. 15. (a) Coil setup of case 1 in Fig. 6(b). Measured (b) k, (c) current amplitude, (d) current phase, (e) η_{SYS}, and (f) load power with different lateral misalignments. Two conventional methods and the proposed method are compared.

k_{4A} are discussed and the same conclusion can be drawn for k_{1A} and k_{2A}.

When $x = 0$ mm, as shown in Fig. 15(b), k_{3A} and k_{4A} have nearly the same amplitude. According to the control algorithm in Section II-A, the current (I_{3A}) through TX coil 3A and that (I_{4A}) through TX coil 4A should have the same amplitudes; this is confirmed in Fig. 15(c). k_{3A} is positive, whereas k_{4A} is negative. Thus, it is required that I_{3A} and I_{4A} be in antiphase. This is also confirmed in Fig. 15(d). When $x = 12.5$ mm, as shown in Fig. 15(b), the ratio of amplitudes of k_{3A} and k_{4A} is 0.53, which is also the required ratio of amplitudes of I_{3A} and I_{4A}. This requirement is confirmed by the measured value (0.56), as shown in Fig. 15(c). In Fig. 15(d), I_{3A} and I_{4A} are in antiphase, which is in accordance with the polarities of k_{3A} and k_{4A}.

More discussions about k_{1A} and k_{2A} are given for $x = 12.5$ mm. In Fig. 15(b), k_{2A} shows some difference from k_{4A}, which is ascribed to the fact that the experimental setup is not perfectly symmetrical. However, that does not affect the operation of the AMFA ICs. From Fig. 15(b) and (c), the ratio of amplitudes of the current (I_{1A}) through TX coil 1A and the current (I_{2A}) through TX coil 2A is 0.72, which is approximately equal to the ratio of k_{1A} to k_{2A} (0.67). In addition, I_{1A} and I_{2A} are in antiphase, which is determined by the polarities of k_{1A} and k_{2A}.

Thus, the current through each TX coil is proportional to k between the TX coil and the RX coil. Our experiment copes with the analysis in Section II-A, which guarantees a good performance of our WPT system. Fig. 15(e) and (f) shows η_{SYS} (the ratio of the load power to the input power from dc supply) and load power measured using different WPT methods. The power consumption of all on-chip digital control is also included. The black curve shows the measured results of driving a single TX coil as shown in Fig. 2(a). TX coils 1A, 2A, and 1A are driven when $x = 0$, 12.5, and 25 mm, respectively. The blue curve shows the measured results by driving four TX coils with the same current, in other words, without control, as shown in Fig. 2(b). Compared with these two conventional methods, the proposed method of driving four TX coils with control, as shown in Fig. 2(c) can significantly improve both η_{SYS} and load power. Take $x = 0$ mm as an example. Compared with the conventional WPT methods, η_{SYS} is improved from 0.02% to 48% and load power is also improved from 0.11 to 458 mW.

Case 2 in Fig. 6(b) is also considered. The experimental results are shown in Fig. 16. After the k-sensing mode, AMFA ICs TX1–TX4 select TX coils 1B, 2A, 3B, and 4A, respectively, and operate in the WPT mode. The same as in case 1, the current through each TX coil is proportional to k between the TX coil and the RX coil. As a result, the WPT performance can be greatly improved by using the proposed method of driving four TX coils with control, compared with the two conventional methods in Fig. 2. Take $x = 0$ mm as an example. η_{SYS} is improved from 0.11% to 51% and load power is also improved from 0.85 to 576 mW. Through cases 1 and 2, it is demonstrated that an independent control can be realized by the selectively activated shared-HB PA topology together with an alternate TX coil array in our WPT system.

Furthermore, to comprehensively evaluate the performance of the proposed WPT system, further analysis is performed. Different representative positions of the RX coil relative to the TX coils are summarized in Fig. 17. Besides the condition that the RX coil is perpendicular to the TX coils, another condition that the RX coil is parallel to the TX coils is also considered. For both conditions, the distance is defined as that from the

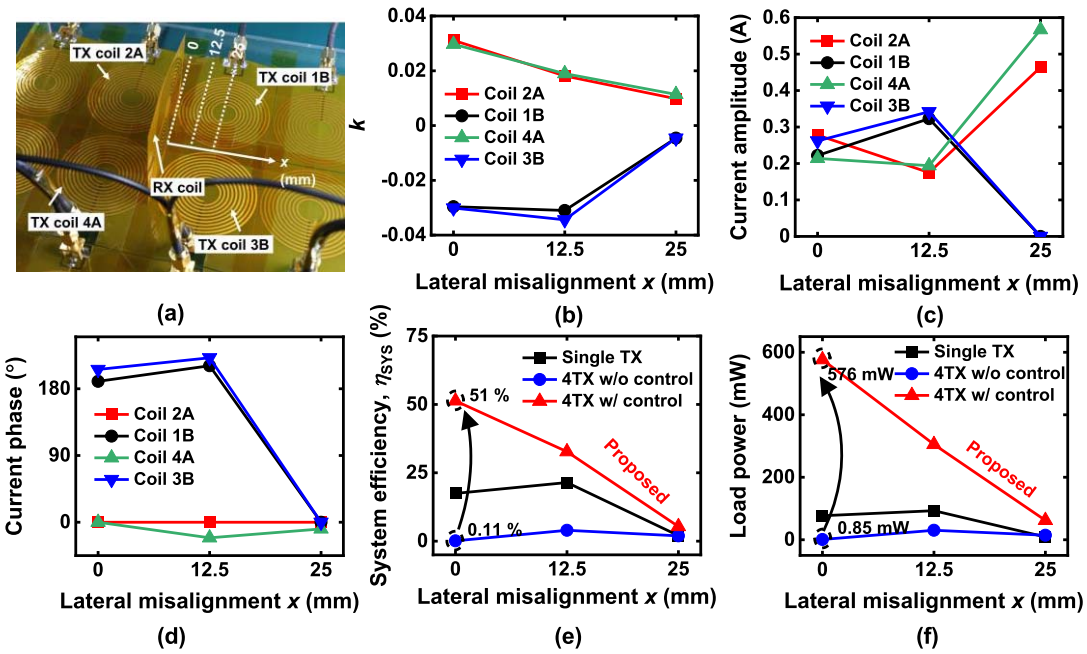

Fig. 16. (a) Coil setup of case 2 in Fig. 6(b). Measured (b) k, (c) current amplitude, (d) current phase, (e) η_{SYS}, and (f) load power with different lateral misalignments. Two conventional methods and the proposed method are compared.

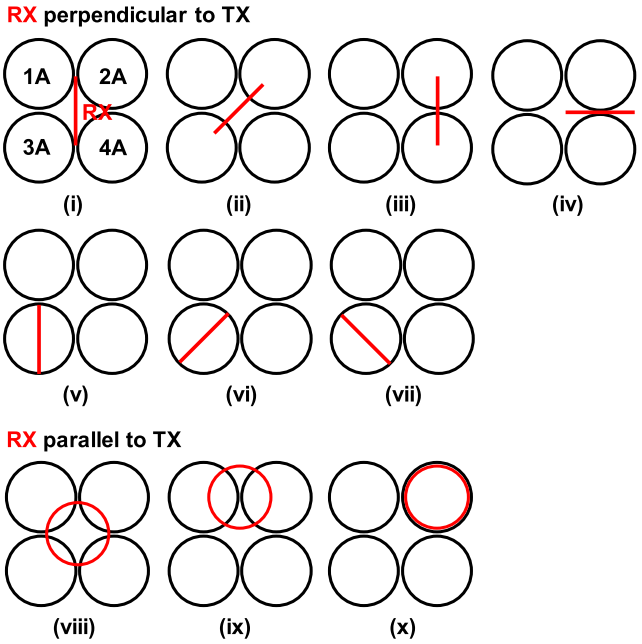

Fig. 17. Top-view schematic of TX (black) and RX (red) coils for different positions of the RX coil.

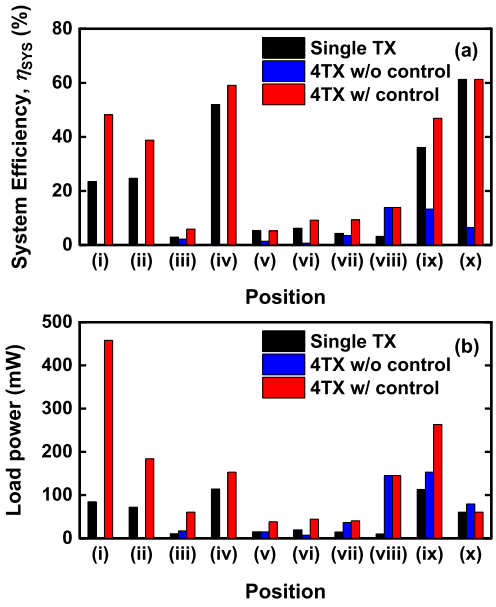

Fig. 18. Measured (a) η_{SYS} and (b) load power corresponding to different positions of the RX coil in Fig. 17.

center of the RX coil to the TX coils. Its value is 25 mm, that is, half the diameter of coils.

Fig. 18 summarizes η_{SYS} and load power measured using three different WPT methods for different positions of the RX coil. The supply voltage was 1.8 V. For all positions, the increase in η_{SYS} by the adoption of the proposed AMFA IC has been demonstrated. More discussions are given for positions (iii) and (v)–(vii). At these positions, the absolute value of k is small and results in a low coil-to-coil efficiency. This is the reason why low values of η_{SYS} and load power are shown even with the adoption of the proposed AMFA IC. For the position (x), in our proposed method, the amplitude of the current in TX coils 1A, 3A, and 4A is smaller than that in TX coil 2A. Thus, compared with driving four TX coils without control, the input power is smaller in our proposed method. This is the reason why a smaller load power but a higher η_{SYS} are shown.

TABLE I
COMPARISONS WITH PREVIOUS WORKS ON CHARGING SINGLE RX COIL USING MULTIPLE TX COILS

		[22]	[25]	This work
Implementation		Discrete	Discrete	180 nm CMOS
TX coil array control		Phase	Amplitude and phase	Amplitude and phase
Number of TX coils		3 x 3	2 x 1	2 x 2
Frequency		460 MHz	13.56 MHz	6.78 MHz
Supply voltage		N/A	10 V	1.8 V
PA topology for multiple TX coils		PA inside VNA	DC-DC + Class-E PA	Selectively activated shared-HB PA
k sensor		VNA	N/A	Integrated TIA
TX ∥ RX	Load power	N/A	1.2 W	55 mW
	WPT efficiency	0.66 %	43 %	63 %
	Distance*/TX size	7	1/2	1/2
TX ⊥ RX	Load power	N/A	N/A	576 mW
	WPT efficiency	N/A	N/A	51 %
	Distance*/TX size	N/A	N/A	1/2

* Distance between the center of the RX coil and TX coils.

Table I shows the performance characteristics of our method and those in previous works on charging a single RX coil using multiple TX coils. Our design realizes the implementation of the AMFA IC for the first time. With our proposed AMFA IC, compared with the conventional WPT methods, the multiple-TX WPT system achieves η_{SYS} improvement from 0.11% to 51% when the RX coil is perpendicular to the TX coils. When the RX coil is parallel to the TX coils, η_{SYS} also compares favorably with those in previous works. One may be curious about why the parallel case shows a higher η_{SYS} but with a smaller load power compared with the perpendicular case. In the parallel case, a high k results in a high R according to (4), that is also the output impedance of a PA. This limits the output power of the PA [16], which results in a small load power shown in the parallel case though with a high η_{SYS}.

More discussions are given. First, on the basis of all measurement results, it can be concluded that the significant performance improvement in the multiple-TX WPT system is worth the effort expended in optimizing the current in each TX coil. Second, the algorithm described in Section II-A was realized using the LabVIEW control block. In future work, the integration of this algorithm is expected to further improve the integration level and bring the WPT system closer to real applications. Third, the load power in this work is below 1 W but enough for the wireless charging of a smart watch. We would like to emphasize that the load power is not limited by our design but by V_{DD}. By choosing another implementation technology with a higher V_{DD}, the load power is expected to be increased to the order of 10 W that can also satisfy the charging requirement for a mobile phone.

V. CONCLUSION

The AMFA IC was implemented, for the first time, in a 6.78-MHz multiple-TX WPT system to enable the control of the amplitude and phase of the current in each TX coil to maximize η_{SYS}. The selectively activated shared-HB PA topology together with an alternate TX coil array was proposed for independent current control in each TX coil. Duty-ratio control guaranteed correct k sensing in the integrated k sensor when k was smaller than 0.12. A WPT system consisting of four AMFA ICs, a 4×4 TX coil array, and a single RX coil was implemented. Measurement results showed that, compared with the conventional system, η_{SYS} was improved from 0.11% to 51% with a load power of 576 mW when the RX coil was perpendicular to the TX coils. A η_{SYS} of 63%, which is higher than those in previous works, was also achieved when the RX coil was parallel to the TX coils. Moreover, η_{SYS} improvement for different positions of the RX coil upon the adoption of the AMFA IC was demonstrated.

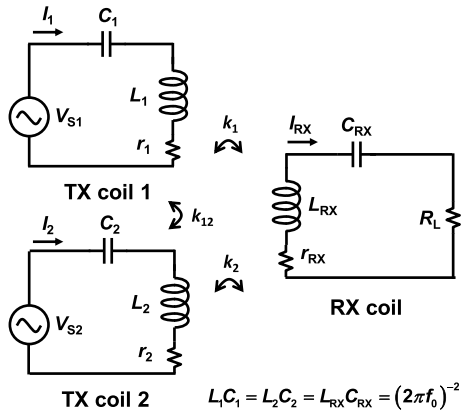

Fig. 19. Equivalent circuits of TX coils 1 and 2, and the RX coil. All coils resonate at the same f_0.

APPENDIX

A. POL of k

To make the analysis simple, we consider a WPT system consisting of TX coils 1 and 2, and the RX coil, as shown in Fig. 19. Since k_{12} is constant and does not change over time, its value can be measured offline prior to the experiment. We pick TX coil 1 as the reference and its POL is positive by definition. Note that its POL could be defined as negative, in which case, the POL of k_2 would flip without any change in power delivered to the RX coil. We assume all k amplitudes were determined by the procedure described in Section III-B.

By applying Kirchhoff's law to the circuit, we can obtain

$$\begin{aligned} V_{S1} &= I_1 r_1 - j\omega_0 k_1 \sqrt{L_1 L_{RX}} I_{RX} + j\omega_0 k_{12} \sqrt{L_1 L_2} I_2 \\ V_{S2} &= I_2 r_2 - j\omega_0 k_2 \sqrt{L_2 L_{RX}} I_{RX} + j\omega_0 k_{12} \sqrt{L_1 L_2} I_1 \\ j\omega_0 k_1 \sqrt{L_1 L_{RX}} I_1 &+ j\omega_0 k_2 \sqrt{L_2 L_{RX}} I_2 = I_{RX}(R_L + r_{RX}) \end{aligned} \tag{7}$$

through which we can derive

$$\frac{\omega_0^2 k_1 \sqrt{L_1 L_{RX}} k_2 \sqrt{L_2 L_{RX}}}{r_{RX} + R_L} = \left[V_{S2} - \left(r_2 + \frac{\omega_0^2 k_2^2 L_2 L_{RX}}{r_{RX} + R_L} \right) I_2 - j\omega_0 k_{12} \sqrt{L_1 L_2} I_1 \right] / I_1. \tag{8}$$

$$\mathrm{POL}(k_1k_2) = \mathrm{POL}\left\{\left[V_{S2} - \left(r_2 + \frac{\omega_0^2 k_2^2 L_2 L_{\mathrm{RX}}}{r_{\mathrm{RX}} + R_L}\right) I_2 - j\omega_0 k_{12}\sqrt{L_1 L_2} I_1\right]/I_1\right\} \tag{9}$$

In the above equation, ω_0, L_1, L_2, L_{RX}, r_1, r_2, r_{RX}, and R_L correspond to the experimental setup and have been known. By measuring V_{S2}, I_1, and I_2, we can determine the POL of k_1k_2 as (9), shown at the top of the page, and thus know the POL of k_2.

After explaining how to determine the POL of k, we explain the details in the experiment as follows. Take TX coils 1A and 2A as examples. Both AMFA ICs TX1 and TX2 operate in the k-sensing mode and the equivalent circuit is the same as that in Fig. 8(b). V_{S1} and V_{S2} in Fig. 19 correspond to the amplitude component of V_{IN} at f_0. I_1 and I_2 can be obtained by substituting the measured V_{OUT} in (5). The phase difference between the current and V_{OUT} is calibrated when the RX coil is absent. Thus, in our experimental setup, the polarities of k_1 and k_2 can be determined and the same principle can apply to a WPT system consisting of more TX coils.

B. Unknown R_L

In this work, we implemented the WPT system using $R_L = 10\ \Omega$. Someone may be concerned whether the system can take care of the case where R_L is unknown or changes during the charging process.

In this section, we first demonstrate that an unknown R_L does not affect the operation of the WPT system.

As discussed in Section II-A, as long as the ratio of optimized I_1 and I_2 equals that of k_1 and k_2, the system efficiency can be maximized. According to (4), R_1 and R_2 can be measured through the k sensor, and their values are correlated with k_1 and k_2, respectively,

$$\begin{aligned} R_1 &= r_1 + \frac{\omega_0^2 k_1^2 L_1 L_{\mathrm{RX}}}{r_{\mathrm{RX}} + R_L} \\ R_2 &= r_2 + \frac{\omega^2 k_2^2 L_2 L_{\mathrm{RX}}}{r_{\mathrm{RX}} + R_L} \end{aligned} \tag{10}$$

where R_1 and R_2 are the equivalent impedances looking into TX coils 1 and 2, respectively.

Through (10), the ratio of the amplitudes of k_1 and k_2 can be determined as

$$\frac{k_1}{k_2} = \sqrt{\frac{L_2}{L_1}}\sqrt{\frac{R_1 - r_1}{R_2 - r_2}}. \tag{11}$$

In (11), L_1, L_2, r_1, and r_2 are the parameters of coils and have been determined prior to the experiment. R_1 and R_2 can be measured by the k sensor in the experiment. Thus, although R_L is not known to the system, the ratio of optimized I_1 and I_2 can be determined as (11). Thus, whether R_L is known or not does affect the operation of our system.

Regarding the POL, we also assume that k_1 is positive and discuss how to determine the POL of k_2. By substituting (10) into (8), we can obtain

$$\mathrm{POL}(k_1k_2) = \mathrm{POL}\left\{\left[V_{S2} - R_2 I_2 - j\omega_0 k_{12}\sqrt{L_1 L_2} I_1\right]/I_1\right\}. \tag{12}$$

Through (12), the POL of k_1k_2 does not require the information of R_L and can be known. Thus, the POL of k_2 can also be determined.

From the above analysis, we have demonstrated that an unknown R_L does not affect the operation of our system. Here, we consider the change of R_L during the charging process, which is common in practice. As discussed in Section II-B, to adapt to the change of the position of the RX coil, our system divides the whole charging process to different time intervals. For each time interval, it is acceptable that R_L is considered a constant. When it goes to the next time interval, R_L changes and our system also adapts to it.

REFERENCES

[1] Z. Zhang, H. Pang, A. Georgiadis, and C. Cecati, "Wireless power transfer—An overview," *IEEE Trans. Ind. Electron.*, vol. 66, no. 2, pp. 1044–1058, Feb. 2019.

[2] B. H. Waters, B. J. Mahoney, G. Lee, and J. R. Smith, "Optimal coil size ratios for wireless power transfer applications," in *Proc. IEEE Int. Symp. Circuits Syst. (ISCAS)*, Jun. 2014, pp. 2045–2048.

[3] T.-H. Kim, G.-H. Yun, W. Y. Lee, and J.-G. Yook, "Asymmetric coil structures for highly efficient wireless power transfer systems," *IEEE Trans. Microw. Theory Techn.*, vol. 66, no. 7, pp. 3443–3451, Jul. 2018.

[4] H. Qiu, T. Sakurai, and M. Takamiya, "Digital transmitter coil for wireless power transfer robust against variation of distance and lateral misalignment," *IEEE Trans. Microw. Theory Techn.*, vol. 68, no. 9, pp. 4031–4039, Sep. 2020.

[5] J. L. Villa, J. Sallan, J. F. S. Osorio, and A. Llombart, "High-misalignment tolerant compensation topology for ICPT systems," *IEEE Trans. Ind. Electron.*, vol. 59, no. 2, pp. 945–951, Feb. 2012.

[6] T. Kan, F. Lu, T.-D. Nguyen, P. P. Mercier, and C. C. Mi, "Integrated coil design for EV wireless charging systems using LCC compensation topology," *IEEE Trans. Power Electron.*, vol. 33, no. 11, pp. 9231–9241, Nov. 2018.

[7] L. Zhao, D. Thrimawithana, and U. K. Madawala, "Hybrid bidirectional wireless EV charging system tolerant to pad misalignment," *IEEE Trans. Ind. Electron.*, vol. 64, no. 9, pp. 7079–7086, Sep. 2017.

[8] X. Li, C.-Y. Tsui, and W.-H. Ki, "A 13.56MHz wireless power transfer system with reconfigurable resonant regulating rectifier and wireless power control for implantable medical devices," *IEEE J. Solid State Circuits*, vol. 50, no. 4, pp. 978–989, Apr. 2015.

[9] L. Cheng *et al.*, "A 6.78-MHz single-stage wireless charger with constant-current constant-voltage charging technique," *IEEE J. Solid-State Circuits*, vol. 55, no. 4, pp. 999–1010, Apr. 2020.

[10] H. S. Gougheri and M. Kiani, "Self-regulated reconfigurable voltage/current-mode inductive power management," *IEEE J. Solid-State Circuits*, vol. 52, no. 11, pp. 3056–3070, Nov. 2017.

[11] F. Mao, Y. Lu, and R. P. Martins, "A reconfigurable cross-connected wireless-power transceiver for bidirectional device-to-device wireless charging," *IEEE J. Solid-State Circuits*, vol. 54, no. 9, pp. 2579–2589, Sep. 2019.

[12] S.-U. Shin, M. Choi, S. Jung, H.-M. Lee, and G.-H. Cho, "A time-interleaved resonant voltage mode wireless power receiver with delay-based tracking loops for implantable medical devices," *IEEE J. Solid-State Circuits*, vol. 55, no. 5, pp. 1374–1385, May 2020.

[13] H. Kennedy, R. Bodnar, T. Lee, and W. Redman-White, "A self-tuning resonant-inductive-link transmit driver using quadrature symmetric delay trimmable phase-switched fractional capacitance," *IEEE J. Solid-State Circuits*, vol. 53, no. 6, pp. 1694–1706, Jun. 2018.

[14] J. Pan, A. A. Abidi, D. Rozgic, H. Chandrakumar, and D. Markovic, "22.7 an inductively-coupled wireless power-transfer system that is immune to distance and load variations," in *IEEE Int. Solid-State Circuits Conf. (ISSCC) Dig. Tech. Papers*, Feb. 2017, pp. 382–383.

[15] A. P. Sample, D. T. Meyer, and J. R. Smith, "Analysis, experimental results, and range adaptation of magnetically coupled resonators for wireless power transfer," *IEEE Trans. Ind. Electron.*, vol. 58, no. 2, pp. 544–554, Feb. 2011.

[16] T. C. Beh, M. Kato, T. Imura, S. Oh, and Y. Hori, "Automated impedance matching system for robust wireless power transfer via magnetic resonance coupling," *IEEE Trans. Ind. Electron.*, vol. 60, no. 9, pp. 3689–3698, Sep. 2013.

[17] J. P. W. Chow, N. Chen, H. S. H. Chung, and L. L. H. Chan, "An investigation into the use of orthogonal winding in loosely coupled link for improving power transfer efficiency under coil misalignment," *IEEE Trans. Power Electron.*, vol. 30, no. 10, pp. 5632–5649, Oct. 2015.

[18] K. Lee, Z. Pantic, and S. M. Lukic, "Reflexive field containment in dynamic inductive power transfer systems," *IEEE Trans. Power Electron.*, vol. 29, no. 9, pp. 4592–4602, Sep. 2014.

[19] W. X. Zhong, X. Liu, and S. Y. R. Hui, "A novel single-layer winding array and receiver coil structure for contactless battery charging systems with free-positioning and localized charging features," *IEEE Trans. Ind. Electron.*, vol. 58, no. 9, pp. 4136–4144, Sep. 2011.

[20] X. Liu and S. Y. Hui, "Simulation study and experimental verification of a universal contactless battery charging platform with localized charging features," *IEEE Trans. Power Electron.*, vol. 22, no. 6, pp. 2202–2210, Nov. 2007.

[21] G. Yang, M. R. V. Moghadam, and R. Zhang, "Magnetic MIMO signal processing and optimization for wireless power transfer," *IEEE Trans. Signal Process*, vol. 65, no. 11, pp. 2860–2874, Jun. 2017.

[22] B. Zhao, N.-C. Kuo, and A. M. Niknejad, "A gain boosting array technique for weakly-coupled wireless power transfer," *IEEE Trans. Power Electron.*, vol. 32, no. 9, pp. 7130–7139, Sep. 2017.

[23] K. Tomita, R. Shinoda, T. Kuroda, and H. Ishikuro, "1-W 3.3–16.3-V boosting wireless power transfer circuits with vector summing power controller," *IEEE J. Solid-State Circuits*, vol. 47, no. 11, pp. 2576–2585, Nov. 2012.

[24] P. Si, A. P. Hu, S. Malpas, and D. Budgett, "A frequency control method for regulating wireless power to implantable devices," *IEEE Trans. Biomed. Circuits Syst.*, vol. 2, no. 1, pp. 22–29, Mar. 2008.

[25] B. H. Waters, B. J. Mahoney, V. Ranganathan, and J. R. Smith, "Power delivery and leakage field control using an adaptive phased array wireless power system," *IEEE Trans. Power Electron.*, vol. 30, no. 11, pp. 6298–6309, Nov. 2015.

[26] Z. Yan *et al.*, "Efficiency improvement of wireless power transfer based on multi-transmitter system," *IEEE Trans. Power Electron.*, vol. 35, no. 9, pp. 9011–9023, Sep. 2020.

[27] D.-H. Kim and D. Ahn, "Maximum efficiency point tracking for multiple-transmitter wireless power transfer," *IEEE Trans. Power Electron.*, vol. 35, no. 11, pp. 11391–11400, Nov. 2020.

[28] S. Huh and D. Ahn, "Two-transmitter wireless power transfer with optimal activation and current selection of transmitters," *IEEE Trans. Power Electron.*, vol. 33, no. 6, pp. 4957–4967, Jun. 2018.

[29] H. Qiu, T. Sai, and M. Takamiya, "A 6.78 MHz wireless power transfer system enabling perpendicular wireless powering with efficiency increase from 0.02% to 48.2% by adaptive magnetic field adder IC integrating shared coupling coefficient sensor," in *Proc. IEEE Symp. VLSI Circuits*, Jun. 2020, pp. 1–2.

[30] D. Gilabert-Palmer *et al.*, "Measuring coupling coefficient of windings with dissimilar turns' number or tight coupling using resonance," *IEEE Trans. Power Electron.*, vol. 33, no. 11, pp. 9790–9802, Nov. 2018.

[31] F. Farajizadeh, D. M. Vilathgamuwa, D. Jovanovic, P. Jayathurathnage, G. Ledwich, and U. Madawala, "Expandable N-legged converter to drive closely spaced multitransmitter wireless power transfer systems for dynamic charging," *IEEE Trans. Power Electron.*, vol. 35, no. 4, pp. 3794–3806, Apr. 2020.

[32] J. Shin *et al.*, "Design and implementation of shaped magnetic-resonance-based wireless power transfer system for roadway-powered moving electric vehicles," *IEEE Trans. Ind. Electron.*, vol. 61, no. 3, pp. 1179–1192, Mar. 2014.

[33] M. K. Kazimierczuk, *RF Power Amplifiers*, 2nd. ed. Chichester, U.K.: Wiley, 2015.

[34] M. Fu, H. Yin, X. Zhu, and C. Ma, "Analysis and tracking of optimal load in wireless power transfer systems," *IEEE Trans. Power Electron.*, vol. 30, no. 7, pp. 3952–3963, Jul. 2015.

[35] H. Qiu, Y. Narusue, Y. Kawahara, T. Sakurai, and M. Takamiya, "Distance detection system for digital transmitter coil achieving distance-variation-tolerant wireless power transfer," in *Proc. IEEE 15th Brazilian Power Electron. Conf. 5th IEEE Southern Power Electron. Conf. (COBEP/SPEC)*, Dec. 2019, pp. 830–835.

[36] *1 MSPS, 12-Bit Impedance Converter, Network Analyzer*, document AD5933 datasheet, Analog Devices, Sep. 2005.

[37] Y. Liu, B. Li, M. Huang, Z. Chen, and X. Zhang, "An overview of regulation topologies in resonant wireless power transfer systems for consumer electronics or bio-implants," *Energies*, vol. 11, no. 7, pp. 1–22, Jul. 2018.

[38] H. Cai, L. Shi, and Y. Li, "Harmonic-based phase-shifted control of inductively coupled power transfer," *IEEE Trans. Power Electron.*, vol. 29, no. 2, pp. 594–602, Feb. 2014.

[39] R. Shinoda, K. Tomita, Y. Hasegawa, and H. Ishikuro, "Voltage-boosting wireless power delivery system with fast load tracker by $\Delta\Sigma$-modulated sub-harmonic resonant switching," in *IEEE Int. Solid-State Circuits Conf. (ISSCC) Dig. Tech. Papers*, Feb. 2012, pp. 288–289.

[40] H. Li, S. Chen, J. Fang, Y. Tang, and M. A. de Rooij, "A low-subharmonic, full-range, and rapid pulse density modulation strategy for ZVS full-bridge converters," *IEEE Trans. Power Electron.*, vol. 34, no. 9, pp. 8871–8881, Sep. 2019.

[41] Maxim Integrated Products. (Sep. 2010). *High-Efficiency Class D Audio Amplifiers Extend Battery Life in Portable Applications*. [Online]. Available: https://www.maximintegrated.com/en/design/technical-documents/tutorials/1/1760.html

Hao Qiu (Member, IEEE) received the B.S. degree in materials science and the M.Eng. degree in electrical engineering from Nanjing University, Nanjing, China, in 2010 and 2013, respectively, and the Ph.D. degree in electrical engineering from The University of Tokyo, Tokyo, Japan, in 2016.

He joined the School of Electronic Science and Engineering, Nanjing University, in 2021, where he is currently an Associate Professor. He was a Researcher with The University of Tokyo from 2017 to 2020. His research interests include integrated power management circuits for wireless powering and energy harvesting and nano-systems based on low-dimensional materials.

Dr. Qiu received the National Science Fund for Excellent Young Scholars in 2021, the First Prize of Science and Technology Award of Jiangsu Province in 2016, and the IEEE Electron Devices Society (EDS) Japan Chapter Student Award in 2016. He was selected as one of the Highly Cited Chinese Researchers by Elsevier in 2021. He served as a Research Fellow for the Japan Society for the Promotion of Science (JSPS) from 2015 to 2017 and a Representative for the Japan Society of Applied Physics (JSAP) from 2016 and 2018.

Takayasu Sakurai (Life Fellow, IEEE) received the Ph.D. degree in electrical engineering (EE) from The University of Tokyo, Tokyo, Japan, in 1981.

In 1981, he joined Toshiba Corporation, Tokyo, where he designed CMOS DRAM, SRAM, RISC processors, DSPs, and SoC Solutions. He has worked extensively on interconnect delay and capacitance modeling known as Sakurai model and alpha power-law MOS model. From 1988 to 1990, he was a Visiting Researcher with the University of California at Berkeley, Berkeley, CA, USA, where he conducted research in the field of VLSI CAD. Since 1996, he has been a Professor with The University of Tokyo, working on low-power high-speed VLSI, memory design, interconnects, ubiquitous electronics, organic IC's, and large-area electronics. He is currently a Professor Emeritus. He was a Domain Research Supervisor for nano-electronics area with the Japan Science and Technology Agency, Kawaguchi, Japan. He has published more than 700 technical publications, including 200 invited presentations and several books, and filed more than 200 patents.

Dr. Sakurai is an IEICE Fellow. He was a recipient of the 2010 IEEE Donald O. Pederson Award in Solid-State Circuits, the 2009 and 2010 IEEE Paul Rappaport Award, the 2010 IEICE Electronics Society Award, the 2009 IEICE Achievement Award, the 2005 IEEE ICICDT Award, the 2005 P&I Patent of the Year Award, the 2004 IEEE Takuo Sugano Award, and four product awards. He is also the Executive Committee Chair of IEEE VLSI Symposia and the Steering Committee Chair of IEEE A-SSCC. He served as the Conference Chair for the Symposium on VLSI Circuits and ICICDT, the Vice Chair for ASPDAC, the TPC Chair for A-SSCC and VLSI Symposium, an Executive Committee Member for ISLPED, and a Program Committee Member for the IEEE International Solid-State Circuits Conference (ISSCC), CICC, A-SSCC, DAC, ESSCIRC, ICCAD, ISLPED, and other international conferences. He delivered keynote speech at more than 50 conferences, including ISSCC, ESSCIRC, and ISLPED. He was an elected Administration Committee Member for the IEEE Solid-State Circuits Society and an IEEE CAS and SSCS Distinguished Lecturer.

Makoto Takamiya (Senior Member, IEEE) received the B.S., M.S., and Ph.D. degrees in electronic engineering from The University of Tokyo, Tokyo, Japan, in 1995, 1997, and 2000, respectively.

In 2000, he joined NEC Corporation, Minato, Japan, where he was engaged in the circuit design of high-speed digital LSIs. He joined The University of Tokyo in 2005, where he is currently a Professor with the Institute of Industrial Science. From 2013 to 2014, he stayed at the University of California at Berkeley, Berkeley, CA, USA, as a Visiting Scholar. His research interests include the digital gate driver and sensor ICs for power electronics and the integrated power management circuits for automotive and industrial applications.

Dr. Takamiya is a member of the Technical Program Committee of the IEEE Symposium on VLSI Circuits and the IEEE Asian Solid-State Circuits Conference. He received the 2009 and 2010 IEEE Paul Rappaport Awards and the Best Paper Award at the 2013 IEEE Wireless Power Transfer Conference. He served on the technical program committees of the IEEE International Solid-State Circuits Conference (ISSCC) from 2015 to 2020 and the IEEE Custom Integrated Circuits Conference from 2006 to 2011. He was the Far East Regional Chair of ISSCC 2020. He was a Distinguished Lecturer of the IEEE Solid-State Circuits Society from 2019 to 2020.